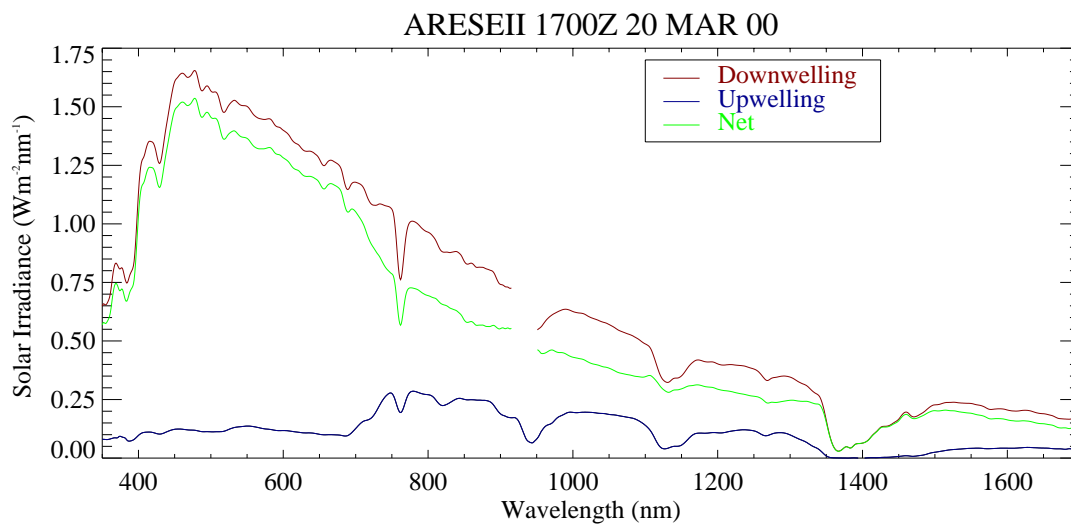
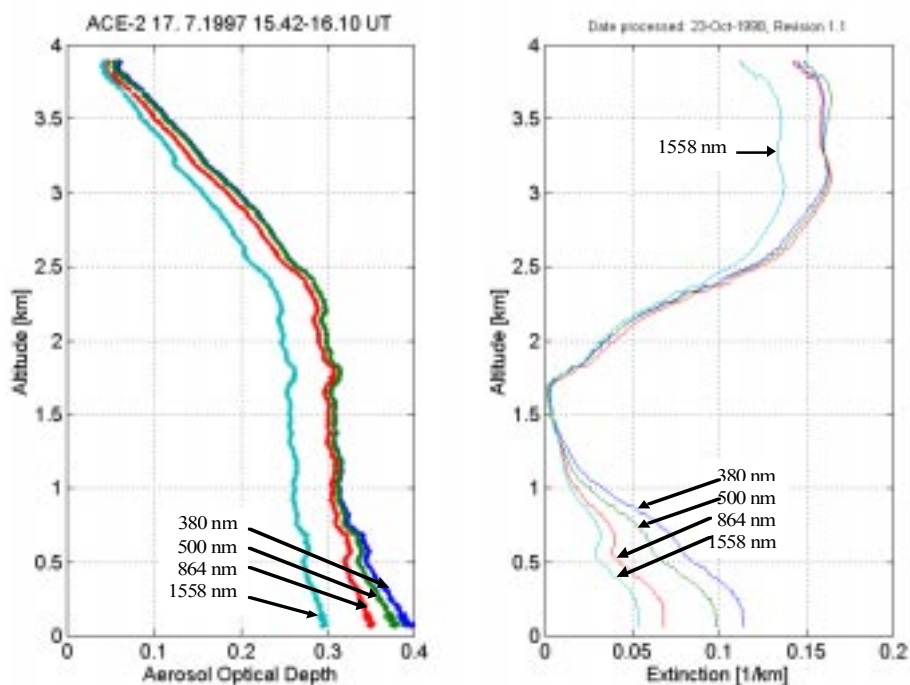


**Figure 1.** Increase of model-measurement bias with water vapor in six discrete spectral bands during the 1997 DOE ARM Shortwave IOP.



**Figure 2.** SSFR downwelling (red) and upwelling (blue) solar spectral irradiance, and the net spectral irradiance (green) at 1700 GMT on 20 March 2000 during ARESEII.



**Figure 3.** Left panel: Profiles of aerosol optical depth at four selected AATS-14 wavelengths (380, 500, 864 and 1558 nm) measured in ACE-2 south of the coast of Tenerife. Right panel: Aerosol extinction profiles derived by differentiating the profiles in the left panel. (Schmid et al., 2000b)

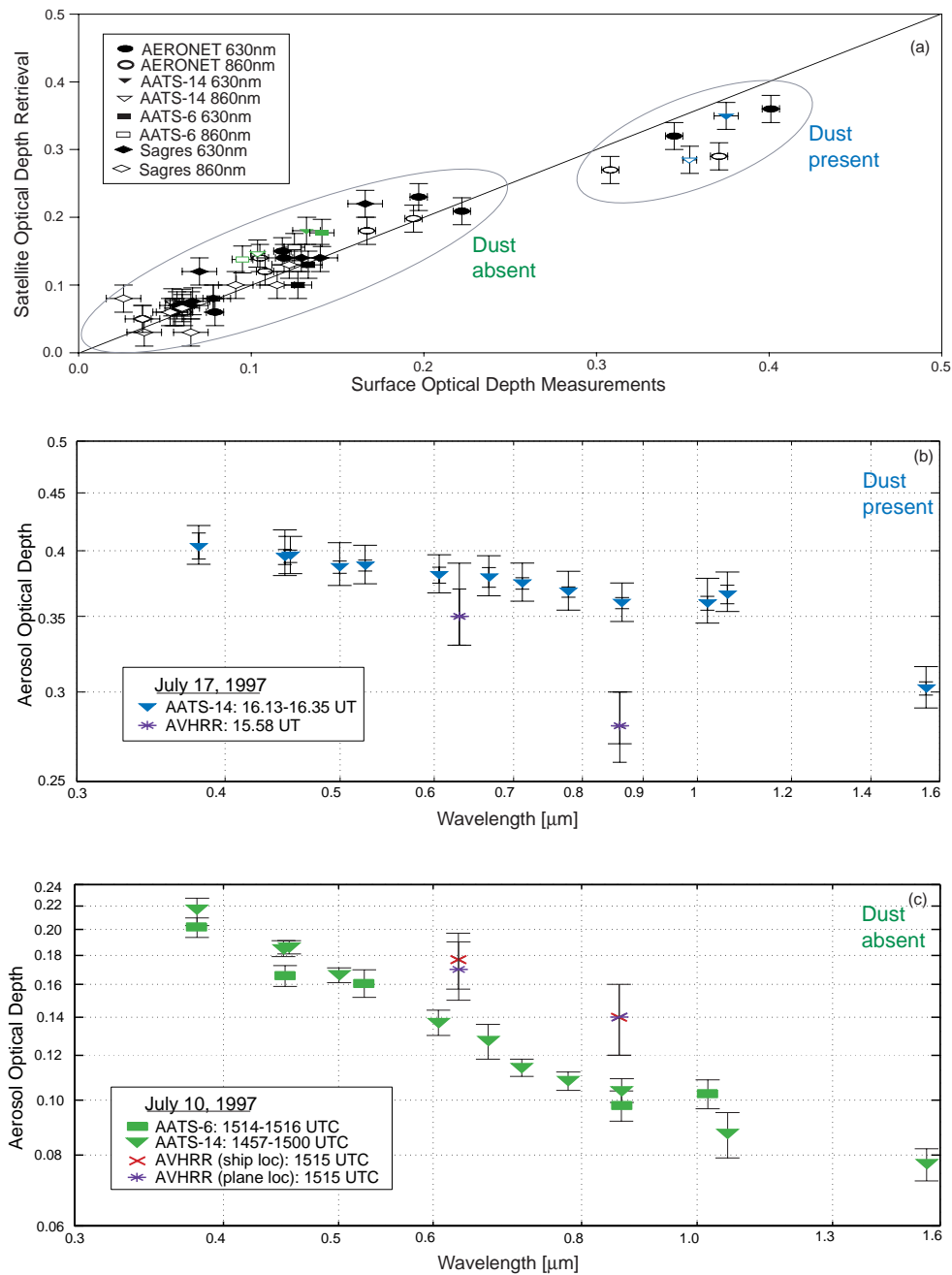


**Figure 4.** (a) Scatter diagram of aerosol optical depth retrieved from AVHRR on the NOAA-14 satellite versus that measured by various photometers at the surface (Durkee et al., 2000). (b) Comparison of aerosol optical depth spectra measured in ACE-2 by AATS-14 on the Pelican aircraft and AVHRR on the NOAA-14 Satellite, July 17, 1997. (Livingston et al., 2000; Schmid et al., 2000). (c) As in (b), for AATS-6 on the R/V Vodyanitskiy ship, AATS-14 on the Pelican aircraft, and AVHRR on the NOAA-14 Satellite, July 10, 1997.

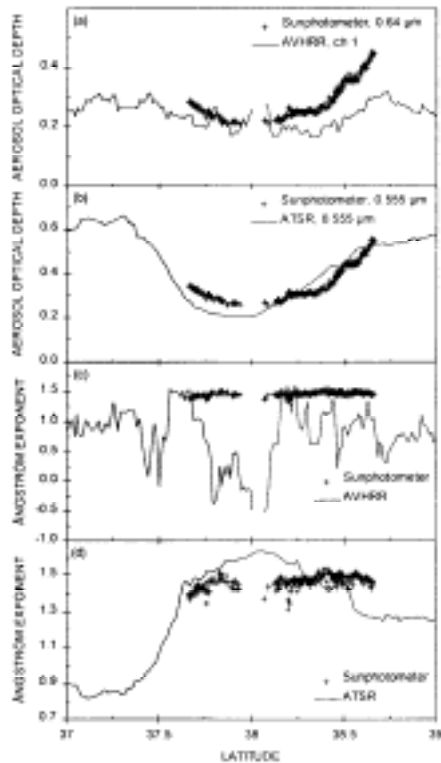


**Figure 5.** Latitude transects of aerosol optical depth and Ångström wavelength exponent as derived from the AATS-6 sunphotometer aboard the UW C-131A, the ATSR-2, and the AVHRR. (a) AVHRR retrieved aerosol optical depth for channel 1 (0.64  $\mu\text{m}$ ) and sunphotometer derived aerosol optical depth at 0.64  $\mu\text{m}$ . (b) same as (a) but for ATSR-2 retrieved aerosol optical depth at 0.525  $\mu\text{m}$  and sunphotometer derived aerosol optical depth at this wavelength; (c) Ångström wavelength exponent as derived from AVHRR and from sunphotometer data; (d) same as (c) but for Ångström wavelength exponent as derived from ATSR-2 and from sunphotometer data (Veefkind et al., 1999).

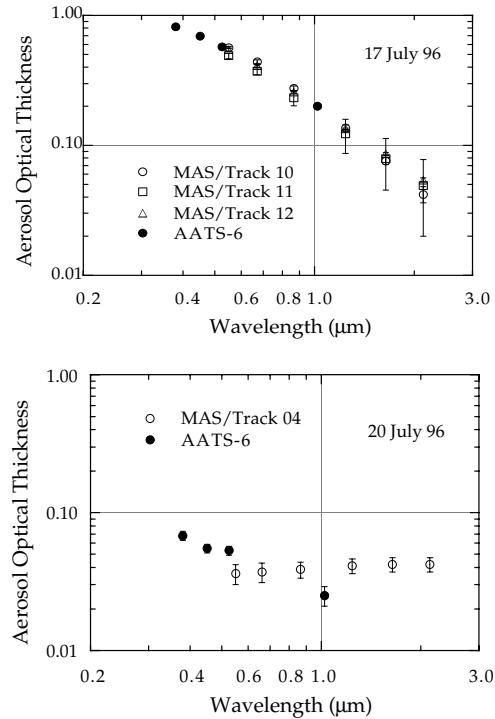


**Figure 6.** Aerosol optical thickness measured by sunphotometer (AATS-6) aboard the C-131A aircraft and derived from MAS data as a function of wavelength. Top frame: Comparison at 37.49°N/74.16°W around 1830UTC. Bottom frame: The sunphotometer data were acquired over point at 38.20°N/73.98°W at 1842UTC. The optical thicknesses derived from the MAS are averaged over a geographical area defined by points located at 38.17°N/74.0°W and 38.27°N/74.1°W; the time of the acquisition was around 1830UTC (Tanre et al., 1999).

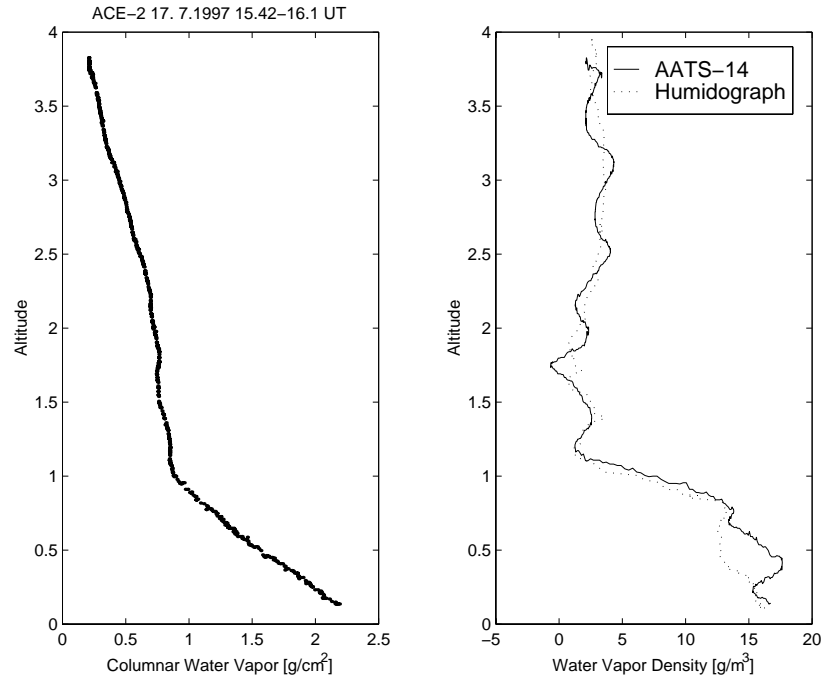


**Figure 7.** Left panel: Profile of the columnar water vapor above the Pelican aircraft measured in ACE-2 south of the coast of Tenerife. Right panel: Water vapor density derived by differentiating the profile in the left panel. Also shown for comparison is the profile obtained by combining readings of a humidograph and outside temperature on Pelican (humidograph data courtesy of S. Gasso, University of Washington). (Schmid et al., 2000)

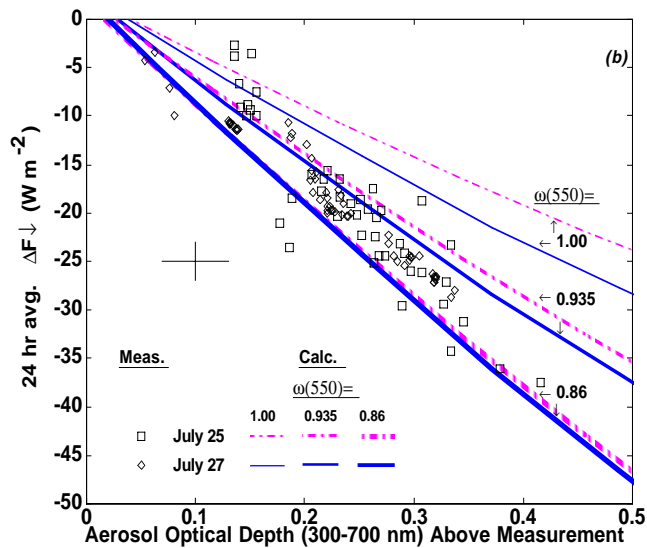


**Figure 8.** Comparison between aerosol-induced change in downwelling solar flux derived from C-130 pyranometer measurements (data points) and calculated (curves) for size distributions retrieved from sunphotometer optical depth spectra using an aqueous sulfate real refractive index and a range of imaginary indexes to give the  $\omega(550)$  values shown. The error bar (cross) shows the uncertainty in flux change and broadband visible optical depth determined from the C-130 pyranometer measurements (Russell, et al., 1999b).

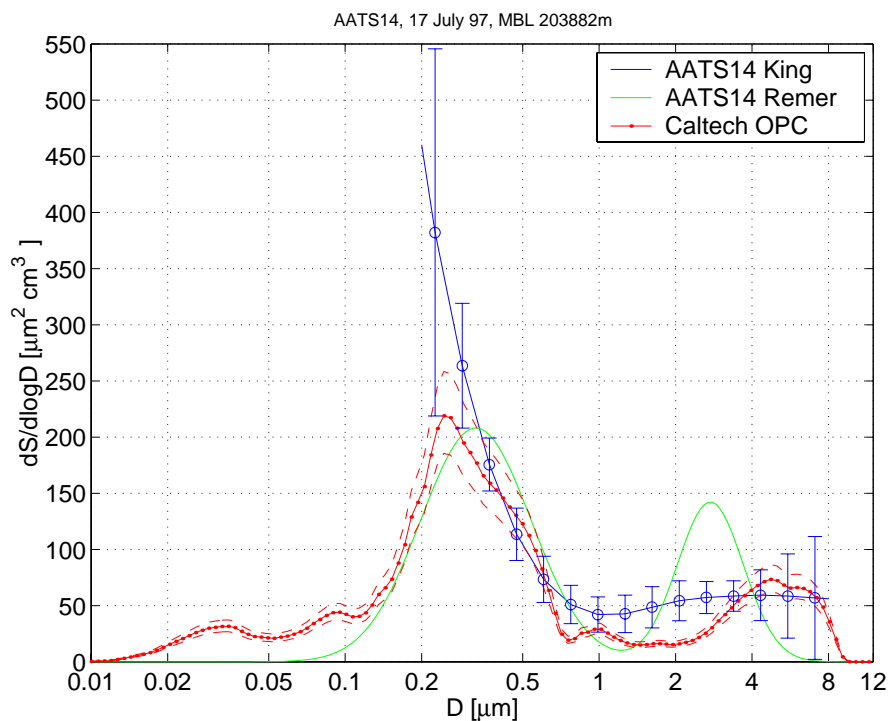


**Figure 9.** Comparison of marine boundary layer aerosol size distributions from in situ measurements and inverted from AATS-14 extinction spectra measured on Pelican flight tf15 in ACE 2 on July 17, 1997. Dashed lines indicate uncertainty of the in situ results (Schmid et al., 2000).

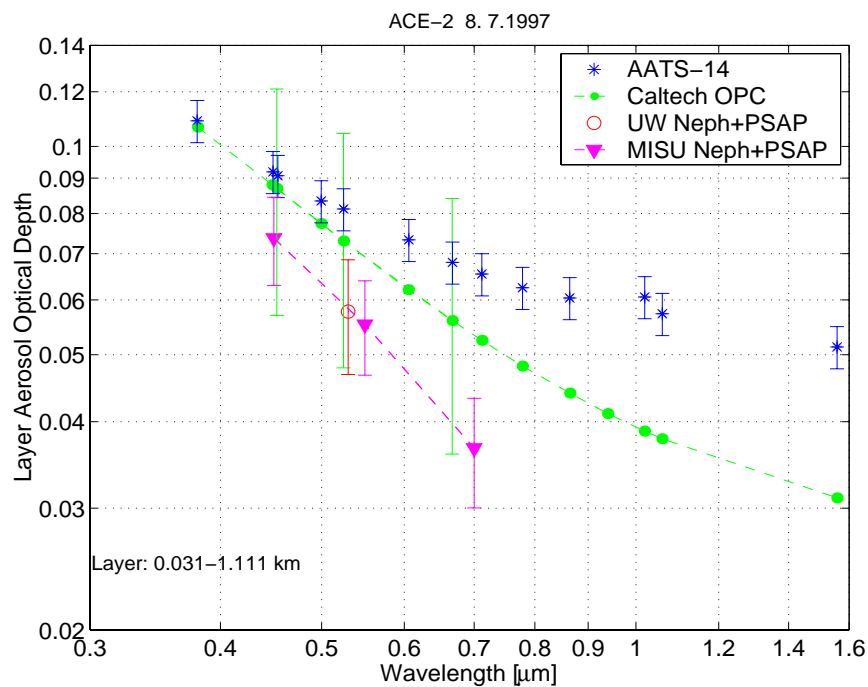


**Figure 10.** Comparison of aerosol optical depth spectra for the marine boundary layer (31-1111 m) during Pelican flight tf20 in ACE 2 on July 8, 1997 (Schmid et al., 2000).